J. Appl. Comput. Mech., 10(1) (2024) 38-54
DOI: 10.22055/jacm.2023.43942.4146

ISSN: 2383-4536
jacm.scu.ac.ir

Shahid Chamran University of Ahvaz

Journal of Applied and Computational Mechanics

Research Paper

Assessment of the Turbine Location for Optimum Performance of the Solar Vortex Engine as a Replacement to the Tall Chimney Solar Updraft Power Plant Design

Ali M. Tukkee[1,2], Hussain H. Al-Kayiem[3], Syed I.U. Gilani[1]

[1] Department of Mechanical Engineering, Universiti Teknologi PETRONAS, 32610 Bandar Seri Iskandar, Perak, Malaysia

[2] Air Conditioning and Refrigeration Techniques Engineering Department, University of Warith Al-Anbiyaa, Karbala 56001, Karbala-Baghdad Rd, Iraq

[3] Hilla University College, Babylon, Iraq

Received May 31 2023; Revised August 28 2023; Accepted for publication August 29 2023.
Corresponding author: A.M. Tukkee (ali_19001829@utp.edu.my)

Abstract. The solar vortex engine (SVE) aims to replace the tall and expensive chimney structure in solar updraft power plants by a shorter less expensive structure named the vortex generator. In this study, the entire SVE system is simulated by CFD to determine the appropriate location for the turbine unit as well as prove the capability of the vortex generator in replacing the chimney. Three different cases for the SVE are considered and compared to corresponding cases of the solar chimney power plant (SCPP). Results revealed that the optimum turbine location is at the outlet hole of the vortex generator. An updraft air velocity of 1.82 m/s was achieved at the outlet hole, compared to 1.56 m/s at the base of a solar chimney with the same diameter as the upper hole. The consideration of the turbine pressure drop did not affect the formation and preservation of the air vortex. So, the 1 m high vortex generator successfully replaced the 8.6 m chimney component in solar updraft power plants, greatly reducing the cost and construction complexity of the plant. The vortex generator accelerated the air delivered from the solar collector, increasing its velocity by 14 times. The SVE's power output is directly proportional to the static pressure drop across the turbine. The mean difference values along the air vortex field between the cases with and without a turbine are 0.67 Pa and 0.026 m/s for the static pressure drop and velocity magnitude, respectively.

Keywords: Vortex generator, Solar chimney, Solar updraft, Solar thermal, Wind turbine.

1. Introduction

Numerous technologies harness energy from the sun for electric power generation. They are divided into direct conversion presented by solar photovoltaic cells and indirect conversion or solar thermal systems. Solar thermal systems also fall under two main categories, concentrated solar power systems and updraft solar power systems. Although concentrated solar systems have higher energy conversion efficiencies, updraft systems are more straightforward and are operated at much lower temperatures. They also have the advantage of being operatable with direct and diffuse solar radiation, unlike concentrating systems that can only benefit from direct solar radiation. This gives solar updraft power plants the advantage of being suitable for more diverse climates than concentrated solar power plants.

The solar chimney power plant (SCPP) is the most widely known solar updraft technology, being of interest to researchers since the 1980s. The SCPP consists of three components: the solar collector, chimney structure and wind turbine. The ground absorbs direct and diffuse solar radiation, and the air is heated under the canopy of the solar collector by absorbing thermal energy from the ground. The heated air moves upward by the stack effect through the tall chimney structure, located at the center of the large solar collector, creating a pressure difference. A wind turbine is used to convert the energy of the air into mechanical work. The wind turbine is usually installed at the bottom of the chimney. Suggestions have also been made to use multiple vertical axis turbines at the bottom of the chimney or multiple horizontal axis turbines under the solar collector canopy and surrounding the chimney [1].

A small-scale prototype was established in 1982 in Manzanares/Spain to evaluate the concept, and the evaluation results were reported by Haaf et al. [2] and Haaf [3]. The Manzanares SCPP consists of a 244 m diameter solar collector with a 194.6 m high chimney. A particular type of wind turbine that, like hydro turbines, operates on static pressure was used as the power generation unit. The turbine blades were adjustable to capture the maximum possible energy from the airflow. The plant successfully generated electric power with a peak output of 50 kW [4].

Colossal engineering and financial challenges when constructing SCPPs lie in the very high and narrow chimney structure.

Published online: September 26 2023

According to Schlaich et al. [4], the plant's power output is directly influenced by the chimney's height. A 100 MW plant is estimated to have a 1000 m high chimney with a diameter of 110 m and a solar collector that is 4300 m in diameter. The construction of a chimney higher than 1000 m would be costly and hard to be achieved with current technology. So, to produce higher power output than 100 MW, the diameters of both the solar collector and chimney must be increased, which requires more land area for the already large power plant.

Another solar updraft power generation concept was proposed by Michaud [5]. This technology uses the same principle as the SCPP, with the significant difference in the air vortex column replacing the chimney. This concept significantly reduces the plant's cost and allows for more power output unaffected by the limitation imposed by the chimney's height. Yet, the technology is still young, and only a few research have been presented on its development.

Solar vortex power plants (SVPPs) are more diverse in design than traditional SCPPs. They all share the same feature of using guide vanes with differences in shape, size and location to generate the air vortex. Few designs for SVPPs have been proposed and investigated by researchers. Most use guide vanes below the solar collector canopy to generate the vortex flow. The research presented for SVPPs concentrated on the plant's design and the system's capability to generate the air vortex. Michaud [6] presented a solar vortex power generation design named the atmospheric vortex engine. The system has multiple inlets at its perimeter where multiple horizontal axis wind turbines can be installed. Natarajan [7] evaluated the system by CFD simulation without considering the turbine unit. He used a transient solution to investigate the air vortex as well as the crosswind effect on its generation and preservation.

Ninic and Nizetic [8] presented another design called the solar power plant with short diffuser. The guide vanes are fixed under the solar collector canopy, and the air vortex leaves the collector to a short diffuser structure at the center of the collector. The turbine could be installed at a specific location inside the short diffuser. CFD simulations were presented by Nizetic et al. [9] and Penga et al. [10] to prove the concept, but no power generation unit was included in these studies.

CFD simulation was used to present and evaluate other solar vortex systems, in which suggestions were made to fix the turbine in an open region inside the vortex field. Zhang et al. [11] presented a device capable at creating a vortex field that is similar in its properties to dust devils. They suggested using a helical-type wind turbine situated at the bottom of the air vortex to capture the energy of the air stream. Another device was presented by Mohiuddin and Uzgoren [12], in which the turbine is again fixed in an open region. In both cases, the wind turbine is unbounded and is dominated by the Betz limit, meaning a theoretical maximum efficiency of 59.3% is achieved.

The only available study for a solar vortex power system that included a turbine unit was performed by Simpson et al. [13]. A 1 m diameter small prototype was operated indoor and outdoor. A suggestion was given to design a turbine capable of extracting energy from the core of the vortex field and the rotational flow at the boundaries. A special 6-bladed vertical axis wind turbine was designed and used in their study. They pointed out that the energy extracted from the axial flow at the core of the air vortex is subjected to the Betz limit.

Al-Kayiem and Mustafa [14] presented a different solar vortex design named the solar vortex engine (SVE). An experimental prototype was developed and tested by Al-Kayiem et al. [15] to evaluate the system's capability to generate a vortex field. The experimental system consists of a solar collector and a central structure named the vortex generator, which is responsible for generating the air vortex. Yet, a turbine unit was not considered. The SVE introduced by Al-Kayiem and Mustafa [14] was then extensively studied by CFD simulations. Al-Kayiem et al. [16] investigated the flow field generated by the SVE. Das and Chandramohan [17, 18] optimized some design parameters such as the upper hole diameter and the number of entry slots. Ismaeel et al. [19, 20] modified the vortex generator by extending the height of the entry slots and guide vanes and investigated some operational parameters on the system's performance such as the air velocity and temperature. The vortex generator design was also studied by Al-Kayiem et al. [21] by considering different geometrical modifications. Finally, Tukkee et al. [22, 23] considered the air humidity effect on the vortex properties. In all those simulation studies, only the vortex generator was considered without the solar collector or the wind turbine. The turbine is intended to be installed at the lower part of the vortex generator. A different suggestion was given by Das and Chandramohan [18] to fix the turbine of the SVE above the vortex generator at a certain height where the maximum vorticity magnitude in the flow field is observed. This suggestion causes the turbine to be unbounded and affected by the Betz limit.

There is an apparent lack of studies for the power generation unit of solar vortex systems, as the type and location of the wind turbine have not been thoroughly investigated. Since each system is unique in its design and the properties of the generated vortex field differ, more investigation should be conducted for the appropriate type and location of the wind turbine for each system.

In this study, CFD simulations are presented for three different cases of the SVE to identify the best location for the turbine unit. The three SVE cases are compared to corresponding SCPP cases. It is the first CFD simulation study to consider the entire SVE system. It also addresses the possibility of replacing the tall chimney structure of traditional solar updraft systems with the less expensive and more convenient vortex generator. In addition to the three parts of the SVE, a 2 m high and 1 m diameter exterior domain is also considered in the simulation to analyze the generated air vortex. The investigations in this study are performed using CFD simulations. However, experimental analysis is also performed to gather data for the input and validation of the simulations.

2. Description of the System and Investigation Cases

A schematic of the SVE is presented in Fig. 1 showing the main parts of the system, with a detailed description of the vortex generator. Solar radiation passes through the collector canopy and is absorbed by the ground. Ambient air enters the circular solar collector from its periphery, which is then heated by convection heat transfer from the ground. Black-painted pebbles cover the ground to increase the absorption of solar radiation and work as a heat storage component. The heated air moves upward by buoyancy forces to the vortex generator while more air is sucked through the inlet of the solar collector to take its place. The solar collector has inner and outer diameters of 10.8 m and 1 m, respectively. The canopy of the solar collector consists of Perspex sheets installed on steel frames and tilted by 8.8° to help guide the upward air stream towards the vortex generator at the center. The inlet and outlet heights of the solar collector are 0.2 m and 0.8 m, respectively.

The vortex generator comprises two Aluminum concentric cylinders. The outer cylinder is insulated and has both a diameter and a height of 1 m. It is opened from below to allow the hot air stream to enter the vortex generator. The inner cylinder diameter is 0.9 m with a height of 0.6 m, and it is covered from below, so the air moves to the open region between the two cylinders. The air stream then enters the inner cylinder through eight 0.6 m high and 0.1 m wide entry slots, each followed by a 0.6 m high and 0.35 m long curved guide vane titled by an angle of 25°. The guide vanes transform the linear flow of the air into a rotational motion, generating the vortex field. Both cylinders are covered from the top. The top cover has a 0.3 m in diameter exit hole that allows the air vortex to leave the vortex generator into the atmosphere. The top cover is made from transparent Perspex, while the interior surfaces are painted black. This approach creates a second heat transfer mechanism that adds more thermal energy to the air without increasing the size of the solar collector.

A wind turbine captures the energy of the air flowing through the system. The appropriate location for the wind turbine is investigated in this study by comparison with different SCPP cases. The investigated three cases of the turbine locations are described below:

Case-1:

The original proposal for the turbine location of the SVE is to be installed at the lower zone of the vortex generator, below the inner cylinder. This way, the turbine would be operated by the air flowing to the vortex generator to maintain the vortex field. The SVE performance is compared to a SCPP with a 1 m diameter chimney, which is similar to the vortex generator diameter, to check the validity of the suggestion. The ratio of the chimney height to collector diameter of the Manzanares SCPP is 194.6/244. By adopting the same ratio, the height of the chimney in the current investigation is 8.6 m. In a no-load condition, when the turbine is not considered, the total pressure difference is equal to the dynamic pressure, which is mainly influenced by the velocity of the air. Hence, the updraft velocity of the air is the factor of comparison between the SVE and SCPP.

Case-2:

The chimney diameter to collector diameter ratio of the Manzanares SCPP is 10.16/244. Adopting this ratio for the current solar collector produces a chimney diameter of 0.45 m. Thus, to compare similar dimensions for the SVE, an orifice plate is added at the lower part of the vortex generator with outer and inner diameters of 1 and 0.45 m, respectively. The turbine of the SVE is inside the hole of the orifice plate, which is the same location as Case-1; but with a reduced turbine swept area. The SVE, in this case, is compared to an SCPP with a chimney of 0.45 m diameter and 8.6 m height. This comparison is named Case-2.

Case-3:

Case-3 differs from Case-1 and Case-2 in terms of the location of the wind turbine. In this case, the turbine is situated at the 0.3 m diameter upper hole of the vortex generator, the base of the air vortex. The diameter of the chimney for the compared SCPP is 0.3 m to have the same turbine swept area as the SVE. The height of the chimney is again taken as 8.6 m.

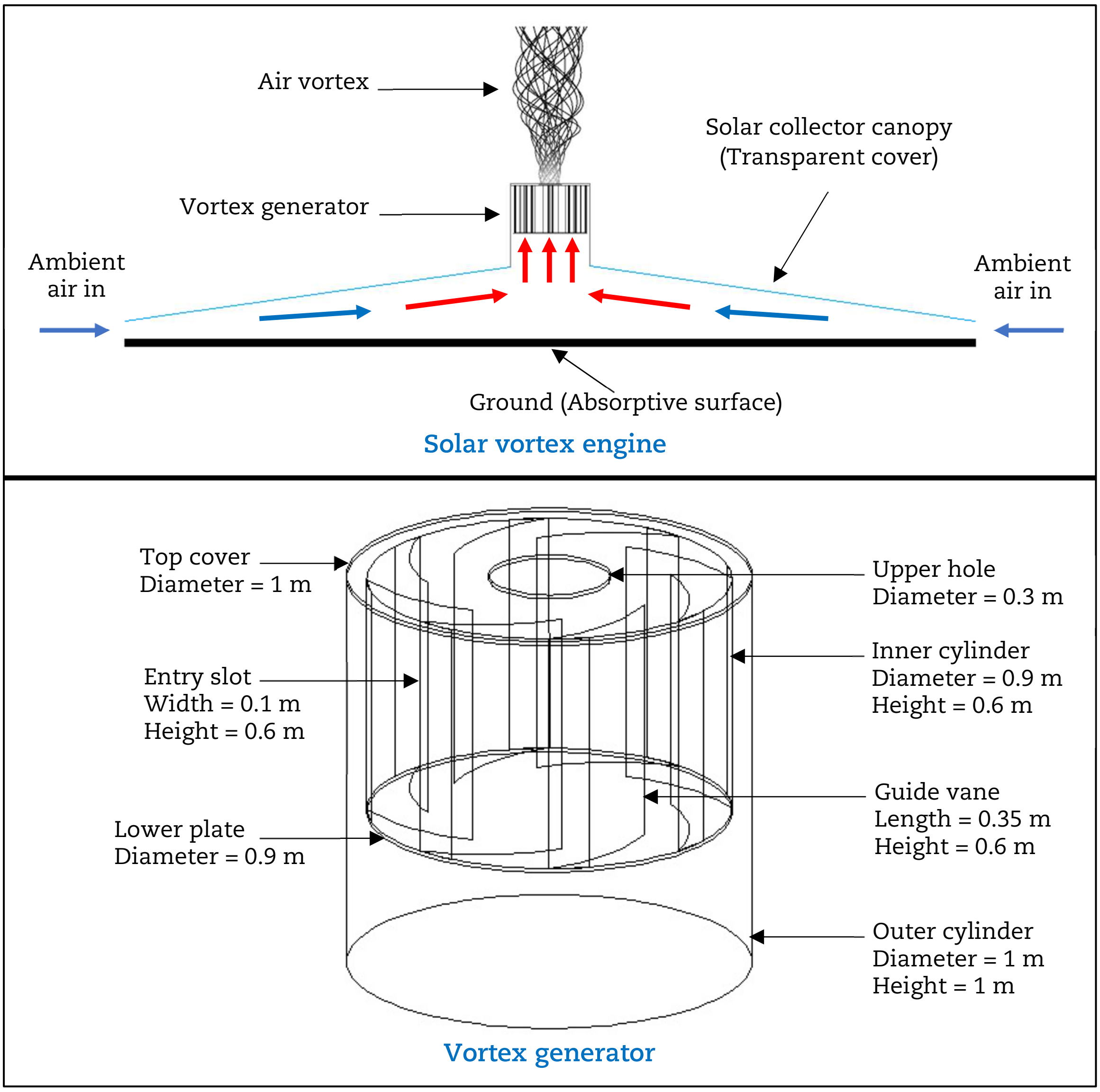

Fig. 1. Schematic showing the principle of the SVE.

Table 1. The investigation cases of the current study with three proposed turbine locations for the SCPP and SVE.

Case	SVE	SCPP
Case-1	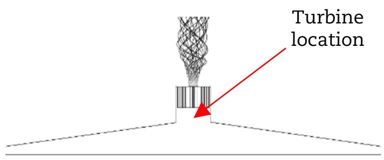 Turbine at the bottom without an orifice plate	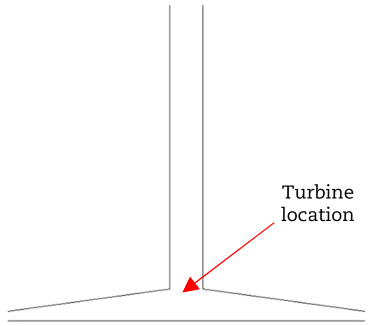 Chimney diameter = 1 m Chimney height = 8.6 m
Case-2	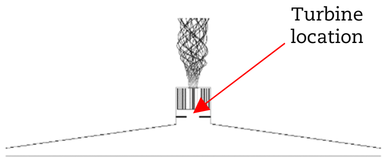 Turbine at the bottom with an orifice plate of 0.45 m diameter	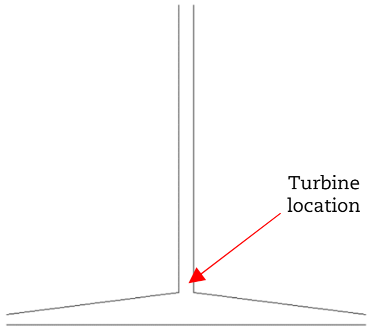 Chimney diameter = 0.45 m Chimney height = 8.6 m
Case-3	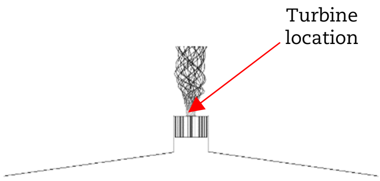 Turbine at the top hole of 0.3 m diameter	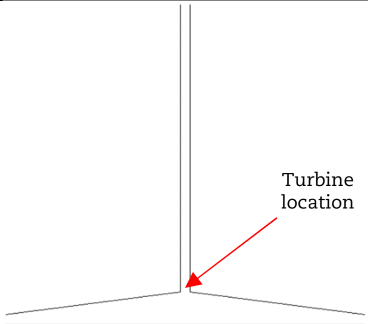 Chimney diameter = 0.3 m Chimney height = 8.6 m

The description of the three considered cases is summarized in Table 1. All of the chosen locations for the turbine unit of the SVE produce bounded turbines, which removes the limitation imposed by the Betz limit for unbounded wind turbines. The three cases were compared with a no-load condition for both the SVE and SCPP. The pressure drop is predicted from the simulation results for each case of the SVE and SCPP.

3. Experimental Methodology

The experimental model of the SVE used for the current investigations is shown in Fig. 2. The system has the dimensions and materials described in section 2 and is not integrated with a wind turbine. It is installed at Universiti Teknologi PETRONAS - Malaysia. Solar and weather data, system temperatures and velocities data were measured from 9:00 AM to 4:00 PM with a one-hour interval between every two recordings. The incident solar radiation was measured using a KIMO-SL 200 solarimeter device. The air velocity at the outlet hole was measured using a KIMO-AMI 300 digital reader with a portable hot wire probe. Thermocouple wires type K were used for measuring the temperatures of the surfaces, while the air temperature at the exit from the upper hole was also recorded using a temperature probe. These were linked a GRAPHTEC GL820 data logger device to record and store the measured temperature values. Three thermocouple wires were used to measure the temperature of the solar absorbing ground; one was fixed at the inlet, one at the outlet, and the third was at the midway of the solar collector. The mean value was calculated and used in the CFD simulation. The variation in the ground temperature readings by the three thermocouples was slight, so using the average value is valid. As for the vortex generator, a thermocouple wire was fixed at a guide vane, one at the center of the lower plate and one at the wall of the inner cylinder. The measurement devices are all calibrated. A weather station provided data for the ambient air temperature and relative humidity.

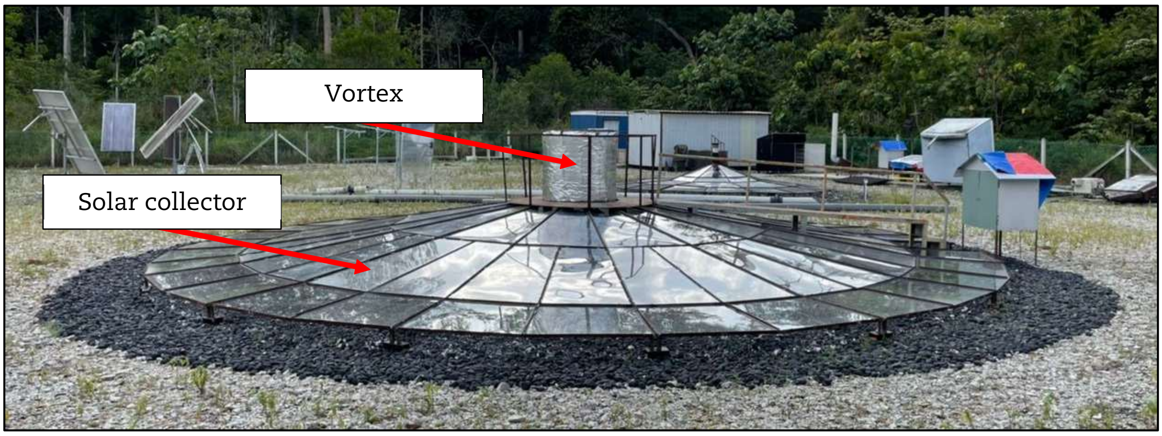

Fig. 2. The experimental prototype of the SVE.

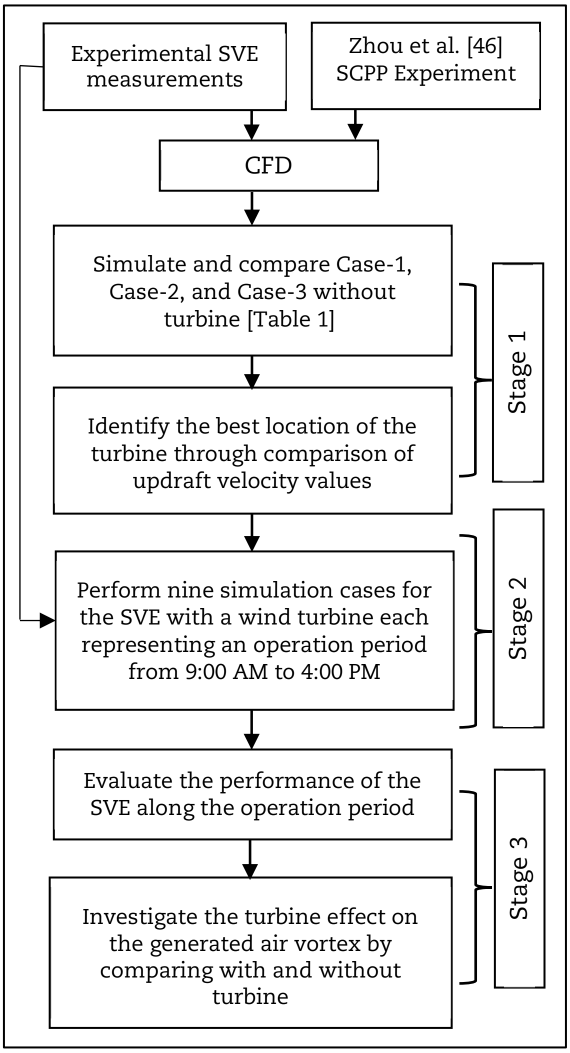

Fig. 3. Execution procedure of the research methodology.

3.1. Uncertainty of Experimental Data

The data acquired from the experimental analysis possess some degree of error as absolutely true measurements cannot be achieved. The error is the difference between the measured and true value [24]. The uncertainty of the temperature measurements is the summation of the uncertainties of the data logger device and the temperature sensors. The data logger uncertainty is ±0.05%, while the thermocouple wire and temperature probes have uncertainty of ±0.75%. So, the total uncertainty of the temperature measurement is (±0.05%) + (±0.75%) = ±0.8%. The maximum measured temperature is 68°C, which gives a maximum uncertainty in the temperature measurements of 68 × (±0.008) = ±0.54°C. As for the air velocity, the combined uncertainty of the hotwire velocity probe and digital reader is ±3%. The maximum measured air velocity is 1.25 m/s, giving a maximum uncertainty in the velocity measurements of 1.25 × (±0.03) = ±0.0375 m/s. The uncertainty of the solarimeter device is ±5%, which represents the error value for the measured incident solar radiation. For the current study, the maximum measured incident solar radiation is 920 W/m^2, which gives a maximum possible uncertainty in the incident solar radiation measurements of 920 × (±0.05) = ±46 W/m^2.

4. CFD Procedure

The objective of this study has been achieved by performing 14 different computational simulation cases. CFD is adopted as it is time consuming and costly if all cases are investigated experimentally. The research included experimental measurements and three consecutive simulation stages. The simulation study's methodology is explained in a flowchart in Fig. 3.

4.1. Creation and Meshing of the Computational Domains

The geometries of the SVE and SCPP computational models were created by AutoCAD. The geometries were then transported to ANSYS DesignModeler. The geometry of the SVE consists of seven parts connected by a shared topology. This enables using a constructed mesh for such a complex geometry. The computational domain of the SVE is shown in Fig. 4. The solar collector was divided into two parts, while the vortex generator consists of 4 parts. An external cylindrical zone of 2 m height and 1 m diameter was also considered as another part. This domain allows for investigating the air vortex outside the vortex generator. This geometry was used for SVE-Cases-1 and SVE-Case-3 since both share the same features, with the difference being in the investigated turbine location. However, for the SVE-Case-2, another computational domain was created with an orifice plate at the base zone of the vortex generator to reduce the area and increase the velocity. The difference in the computational domain of SVE-Case-2 is also shown in Fig. 4.

The geometry of the SCPP is more straightforward and consists of one part. Three computational domains were used for the three different cases. They only differ in the diameter of the chimney structure, as explained earlier. Figure 5 presents the computational domains of the three SCPP cases.

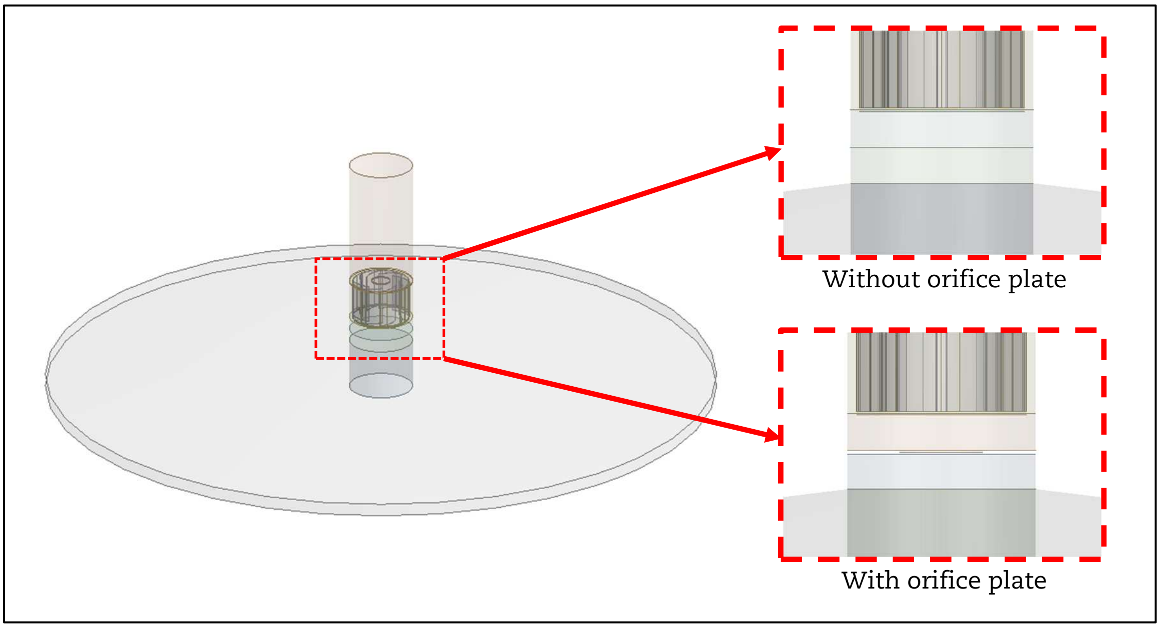

Fig. 4. The computational domains of the SVE simulation cases.

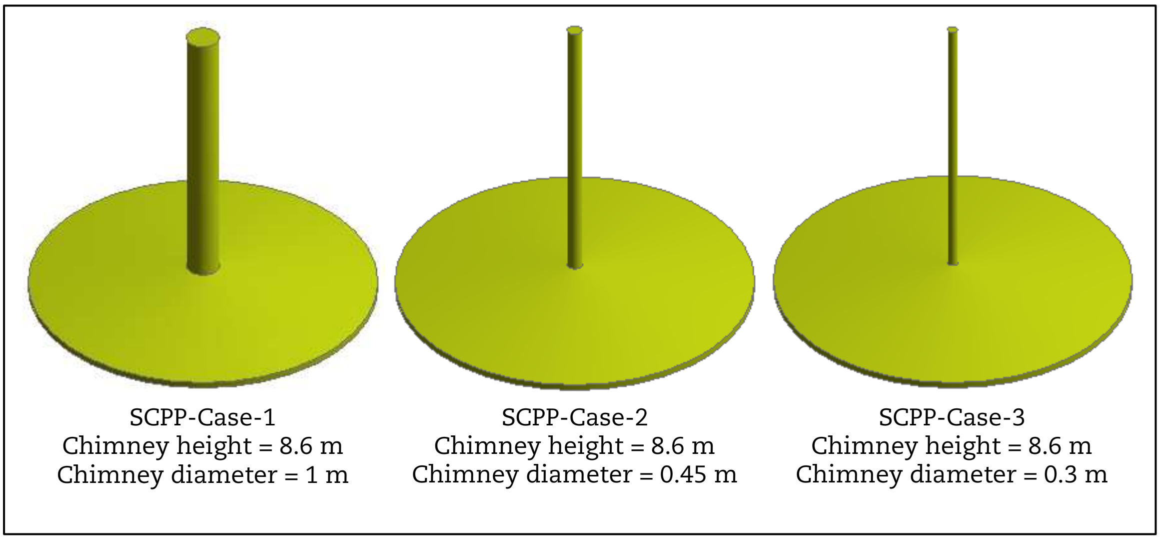

Fig. 5. The computational domains of the SCPP simulation cases.

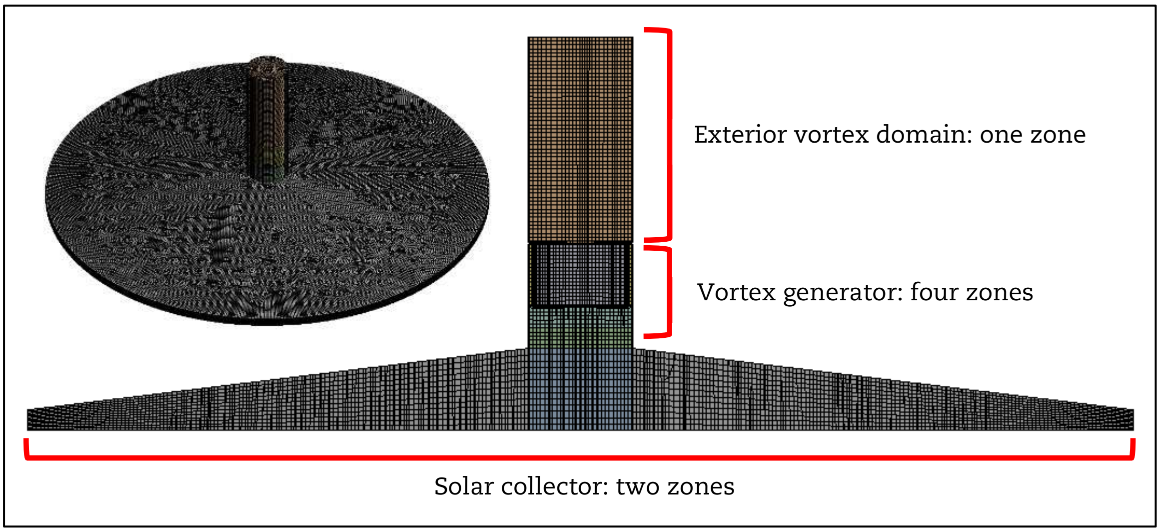

Fig. 6. Multiple zones for the SVE meshed with structured hexahedral cells.

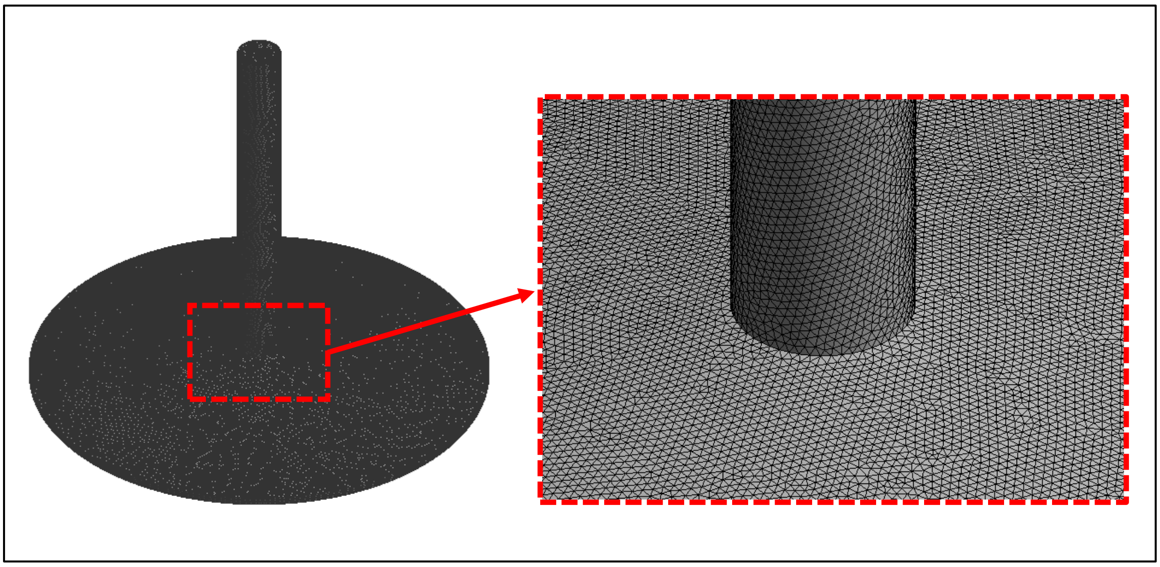

Fig. 7. Single zone for the SCPP meshed with unstructured tetrahedral cells.

ANSYS ICEM was used for meshing the flow domain for all cases. Structured meshing with hexahedral cells and few prism cells were used for the SVE cases. The prism cells produce a higher quality mesh in the curved parts of the system. The multizone method was used for the five zones that comprise the vortex generator and exterior domain, while the sweep method was used for the two zones that form the solar collector. Figure 6 presents a section of the mesh showing the multiple zones of the structured mesh of SVE-Case-1. As for the SCPP cases, unstructured tetrahedral cells were used for meshing the three geometries. A sample of the unstructured mesh of the SCPP cases is shown in Fig. 7. One fine layer was considered in all meshes to make sure that y+ values are in the range required by the turbulence model. Multiple inflation layers were not considered as near-wall functions were adopted for solving the boundary layers, which are explained further in the next section.

Mesh independency studies were performed for SVE-Case-1 and SCPP-Case-1. A comparison was made between the values of the velocity magnitude at the outlet for different meshes. The same cell size acquired from the mesh independency studies for Case-1 was then used for the other simulation cases of the SVE and the SCPP. The summary of the mesh independency studies is presented in Table 2.

Table 2. Mesh independency studies.

Number of cells	Change in predicted outlet velocity
SVE-Case-1	
583207	-
729668	5.5%
904750	3.2%
1137905	0.5%
1359136	0.3%
SCPP-Case-1	
423500	-
563610	7.2%
783428	5.1%
1128432	2.4%
1589556	0.8%

Table 3. Number of cells for each case.

Case	Number of cells
SVE-Case-1 and SVE-Case-3	904750
SVE-Case-2	904792
SCPP-Case-1	1128432
SCPP-Case-2	1008754
SCPP-Case-3	1000869

Table 4. Mesh quality parameters.

Case	Skewness			Orthogonal quality		
	Max.	Min	Avg.	Max.	Min	Avg.
SVE cases 1 and 3	0.72	1.76×10^{-3}	0.11	0.99	0.22	0.98
SVE Case-2	0.71	4.87×10^{-3}	0.12	0.99	0.21	0.98
SCPP Case-1	0.57	1.12×10^{-6}	0.22	0.99	0.42	0.76
SCPP Case-2	0.54	2.45×10^{-6}	0.22	0.99	0.45	0.76
SCPP Case-3	0.64	7.25×10^{-7}	0.22	0.99	0.35	0.76

Although the size of the cells was the same for the other cases, the number of cells vary due to the difference between the geometries of each case. The solutions were considered independent of the mesh size with the number of cells shown in Table 3.

The quality of the mesh for each computational domain is presented in Table 4 through multiple parameters. Low skewness values, close to 0, indicate high-quality cells. In contrast, high orthogonal quality values, close to 1, indicate high-quality cells.

4.2. Assumptions and Governing Equations

The following assumptions were considered for all the simulation cases:

1. Steady state solution for all the computational domains.
2. The flow is turbulent and the working fluid is incompressible.
3. All thermo-physical properties of the working fluid are constant except for the density.
4. The incompressible ideal gas law is used for calculating the density of the air.

ANSYS Fluent solves the governing equations using the finite volume method. All the solved equations will be explained in this section The three conservation equations are expressed as follows [25]:

Conservation of mass:

$$\nabla.(\rho\vec{v}) = S_m \tag{1}$$

Conservation of momentum:

$$\nabla.(\rho\vec{v}\vec{v}) = -\nabla P + \nabla.(\bar{\bar{\tau}}) + \rho\vec{g} + \vec{F} \tag{2}$$

Conservation of energy:

$$\nabla.\left(\vec{v}(\rho E + p)\right) = -\nabla.\left(\sum_j h_j J_j\right) + S_h \tag{3}$$

The realizable $(k-\varepsilon)$ turbulence model was used. This model uses two equations to obtain the kinetic energy and the rate of dissipation of kinetic energy as follows:

$$\frac{\partial}{\partial x_j}(\rho k u_j) = \frac{\partial}{\partial x_j}\left[(\mu + \frac{\mu_t}{\sigma_k})\frac{\partial k}{\partial x_j}\right] + G_k + G_b - \rho\varepsilon - Y_M + S_k \tag{4}$$

$$\frac{\partial}{\partial x_j}(\rho\varepsilon u_j) = \frac{\partial}{\partial x_j}\left[(\mu + \frac{\mu_t}{\sigma_\varepsilon})\frac{\partial \varepsilon}{\partial x_j}\right] + \rho C_1 S\varepsilon - \rho C_2\frac{\varepsilon^2}{k+\sqrt{\nu\varepsilon}} C_{1\varepsilon}\frac{\varepsilon}{k}C_{3\varepsilon}G_b + S_\varepsilon \tag{5}$$

The $(k-\varepsilon)$ turbulence model provides the option for multiple near-wall treatment functions. By using the appropriate function, the need for multiple fine cells near the walls is removed. The near-wall treatment functions cover specific ranges of y+ values. The scalable wall function produced the best convergence with the SVE cases, while the standard wall function was better with the SCPP cases.

Buoyancy forces drive the flow in solar updraft systems and, for this type of flow, the air density varied with temperature. The incompressible ideal gas law was adopted for the density variation in the current study [25, 26]. Thus, the density of the working fluid is calculated from the following law:

$$\rho = \frac{p_{op}}{\frac{R_u}{M_w}T} \tag{6}$$

To add the air humidity, species transport equations were enabled in the Fluent solver and the working fluid was considered as a mixture of air and water vapor [23]. Since the air humidity is very high in Malaysia, where the system is investigated, considering the air humidity is necessary for obtaining accurate results from the CFD simulations. Malaysia's annual relative humidity value ranges from 74% to 86%, with an average value of 80% [27, 28].

Table 5. Properties of the materials used to fabricate the SVE.

Material	Density (kg/m³)	Specific heat (J/kg·K)	Thermal conductivity (W/m·K)
Aluminum	2719	871	202.4
Perspex [29]	1200	1170	0.19
Pebbles [30]	2640	820	1.73

Table 6. Boundary conditions for the SVE cases.

Location	Boundary condition
Solar collector inlet	Mass flow inlet
Ground (absorptive surface)	Constant temperature
Canopy (transparent cover)	Mixed convection and radiation heat transfer
Vortex generator outer cylinder wall	Insulated
Vortex generator inner cylinder wall	Constant temperature
Vortex generator lower cover	Constant temperature
Guide vanes faces	Constant temperature
Vortex generator top cover	Mixed convection and radiation heat transfer
Exterior vortex domain wall	Constant temperature
Vortex domain outlet	Outflow

4.3. Materials and Boundary conditions

The material properties of each component of the SVE and SCPP are shown in Table 5. The absorbing surface is the ground and is covered with black-painted pebbles. The collector canopy and the top of the vortex generator are made from Perspex. All the other surfaces of the vortex generator are made from Aluminum.

The boundary conditions adopted for the SVE models are presented in Table 6. The values of the boundary conditions are taken from the collected experimental data.

The mass flow inlet and outflow boundary conditions were used for the inlet to the solar collector and exit from the exterior vortex zone, respectively. This is because the pressure and velocity of the air at the outlet of the vortex domain are unknown, which promotes the use of the outflow boundary condition. As for the inlet, the outflow boundary condition has a limitation in which an inlet pressure boundary condition cannot be used. This leaves the inlet velocity and inlet mass flow rate options. The air velocity at the inlet to the solar collector is too small and couldn't be measured as it is lower than the minimum limit of the measurement instrument. So, the mass flow rate was calculated at the outlet, and its value was used for the inlet since it is constant along the SVE system operating in a steady state.

The vortex generator's outer cylinder wall was considered insulated, as in the experimental model. Constant temperature values were given for the ground and the vortex generator's inner surfaces. A constant temperature equal to the ambient temperature value was considered for the wall of the exterior vortex domain. This simulates the effect of the ambient air, which can be considered as a constant temperature heat sink.

Mixed convection and external radiation heat transfer boundary conditions were considered for the solar collector canopy and the upper cover of the vortex generator. Convection heat transfer is to the ambient air, while radiation heat transfer is to the sky. The emissivity of Perspex is 0.9 [29], and the external radiation temperature of the canopy and upper cover to the sky is calculated using the Swinbank formula as follows [31]:

$$T_{\text{sky}} = 0.0552 \times T_{\text{o}}^{1.5} \tag{7}$$

The convection heat transfer coefficient for the canopy and the upper cover is calculated as follows [32, 33]:

$$h = 3.87 + 0.0022\left(\frac{V_w \rho C_p}{Pr^{2/3}}\right) \tag{8}$$

The wind velocity in Eq. (8) is taken as 1.64 m/s, which is the mean measured wind velocity value near the solar research site where the experimental data were collected [34].

The inclusion of the turbine effect in a steady state CFD simulation by ANSYS Fluent for SCPPs was performed by two methods. The first method uses the reverse fan boundary condition, which introduces a pressure drop across a certain region presented by an interior surface. The pressure drop can be either a constant value or a function of velocity [35-37]. This method does not consider the geometry of the turbine blades and treats the turbine region as an infinitely thin disc. Since the air velocity does not vary, it is a good method for simulating the type of turbines used in solar updraft power plants, which operate on static pressure drops without changing the flow velocity [4, 38]. The second method uses the multiple reference frame model (MRF) [39-41]. This model allows the inclusion of the turbine geometry. However, it requires an input to the turbine's rotational speed, which cannot be acquired for this study since no experimental model with a turbine unit is available. So, the reverse fan boundary condition was adopted in this study by adding a pressure drop region as a function of the updraft air velocity.

In a no-load condition, the total energy of the air is used for generating the air vortex field, and the total pressure difference is equal to the dynamic pressure:

$$\Delta p_{\text{total}} = \frac{1}{2} \bullet \rho \bullet V^2 \tag{9}$$

When a turbine is considered, the total pressure difference will be divided into static and dynamic components. In this case, the static pressure drop represents the pressure drop across the turbine. So, the total pressure difference becomes:

$$\Delta p_{\text{total}} = \Delta p_{\text{dynamic}} + \Delta p_{\text{turbine}} \tag{10}$$

Table 7. Boundary conditions for the SCPP cases.

Part	Boundary condition
Solar collector inlet	Pressure inlet
Ground (absorptive surface)	Constant temperature
Canopy (transparent cover)	Mixed convection and radiation heat transfer
Chimney wall	Insulated
Chimney outlet	Pressure outlet

Table 8. comparison between the SCPP-Case-3 simulation and the experimental model presented by Zhou et al. [46].

Parameter	Case-3	Experimental model
Solar collector diameter	10.8 m	10 m
Canopy inclination angle	8.8°	8°
Solar collector inlet height	0.2 m	0.05 m
Solar collector outlet height	0.8 m	0.8 m
Chimney diameter	0.3 m	0.3 m
Chimney height	8.6 m	8 m

In SCPPs, the pressure drop across a bounded turbine has been considered by most researchers to be 2/3 of the total pressure difference [38, 42], meaning that:

$$\frac{\Delta p_{\text{turbine}}}{\Delta p_{\text{total}}} = \frac{2}{3} \tag{11}$$

Combining Eq. (9) and Eq. (11) gives:

$$\Delta p_{\text{turbine}} = \frac{1}{3} \bullet \rho \bullet V^2 \tag{12}$$

The pressure drop across the turbine is considered through a reverse fan boundary condition with a polynomial function as follows:

$$\Delta p_{\text{turbine}} = a + b \bullet V + c \bullet V^2 \tag{13}$$

For Eq. (13) to have the same form as Eq. (12), the values of the constants were set as follows:

$$a = b = 0 \tag{14}$$

$$c = \frac{1}{3} \bullet \rho \tag{15}$$

The outlet density in Eq. (15) can be calculated using experimental data. The power output is the product of the pressure drop across the turbine, the volumetric flowrate of the air and the turbine efficiency [4, 36]:

$$P = \eta_{\text{turbine}} \bullet \Delta p_{\text{turbine}} \bullet \dot{V} \tag{16}$$

The turbine efficiency is taken as 0.8 [43, 44]. The boundary conditions adopted for the SCPP cases are shown in Table 7. The same materials were considered for the ground and the canopy, and Eq. (7) and Eq. (8) were used to calculate the sky temperature and convection heat transfer coefficient, respectively. The chimney wall is considered to be insulated. Pressure boundary conditions were used for the inlet of the solar collector and the outlet of the chimney with values of 0 Pa gauge pressure [45].

4.4. Solution Procedure

The solution was carried out using the segregated (SIMPLE) algorithm. This method solves the governing equations sequentially to obtain a converged solution. The convergence of the solution was judged using different criteria. For the SCPP cases, the residuals of the continuity, momentum, turbulence and species transport equations reached 10^{-5}, and the energy equation reached 10^{-6}. As for the SVE cases, the energy equation was again given an accuracy of 10^{-6} while the other residuals reached 10^{-4}. This accuracy is acceptable for such complex flows, and other researchers reported the same accuracy for different solar vortex systems [9, 10]. Another convergence criteria were taken by creating monitors for the velocity, pressure, temperature and density of the air at the outlet of each system. The solution was considered to be converged when these values reached a steady state. Finally, the mass and energy imbalances were checked and found close to zero, indicating a converged solution.

5. Results and Discussion

5.1. Validation of the CFD Simulation Results

The main purpose of the vortex generator is to convert the thermal energy of the air into kinetic energy by increasing its velocity, while the solar collector heats the air entering from the environment increasing its temperature. So, two criteria were chosen for the validation of the simulation results of the SVE, namely the outlet air velocity from the vortex generator and the outlet temperature of the air exiting the solar collector. The results were validated by a comparison between the results of the CFD simulations with the experimental data. The CFD simulation case considered in the comparison is similar to the experimental prototype, i.e., without a turbine or an orifice plate. The maximum outlet air velocity values obtained from the experimental analysis and CFD simulation at 1:00 PM are 1.25 and 1.23 m/s, respectively. In addition, the maximum outlet air temperatures obtained from the experimental analysis and CFD simulation are 48.03 and 49°C, respectively. The slight errors of 1.6 and 2% for the velocity and temperature results, respectively, could be attributed to the uncertainty range of the measurement devices used in the experimental data collection. This closeness between experimental and numerical results proves the validity of the CFD simulation results of the SVE to be used for the current analysis.

Table 9. Area-weighted average velocity at the turbine location for the different cases.

Cases	Velocity at the turbine location (m/s)	
	SVE	SCPP
Case-1	0.13	1.25
Case-2	0.67	1.6
Case-3	1.82	1.56

As for the SCPP cases, there are no available experimental prototypes with the exact dimensions considered in the simulation cases. However, Zhou et al. [46] presented an experimental SCPP model with dimensions very close to Case-3. Table 8 shows a comparison between the dimensions of the two models.

Zhou et al. [46] reported a maximum updraft air velocity in the chimney of 2.13 m/s on a typical warm day in Wuhan city in China. In the current CFD simulation of Case-3, a maximum updraft velocity of 2.035 m/s was obtained at the base of the chimney, as shown in Fig. 8. The two values are very close and comparable, with a percentage difference of 4.46%. Furthermore, the air temperatures at the base of the chimney are 49.2 and 47.1°C for the experimental results and CFD simulation, respectively. This gives a percentage difference of 4.27%. The difference in values can be attributed to the difference in dimensions and the weather conditions in which the two studies were conducted. The other SCPP simulation cases, 1 and 2, achieved the same solution accuracy, which makes them as valid as Case-3 for the current study.

5.2. Analysis of the Turbine Location in the SVE

Three SVE cases are compared to SCPP cases with a corresponding chimney diameter to the location specified for the turbine of the SVE. All the investigated cases are considered without a load, meaning no turbine is considered. The turbine location for the SCPP is considered at 1 m from the ground, the same as the first two SVE cases. The best location for the turbine of the SVE is decided based on the velocity of the air, which determines the pressure drop potential at that location.

Table 9 shows the updraft velocity of the air at the different locations for the SVE and SCPP cases. The area-weighted average velocity values are considered in the comparison. This provides a better indication as it considers the average air velocity along the turbine swept area instead of a specific point. Table 9 shows that the air velocity at the lower part of the SVE is very small compared to the SCPP, Cases 1 and 2, even when considering an orifice plate. As for Case-3, the velocity at the upper hole is higher than that at the 0.3 m diameter chimney. So, the wind turbine's appropriate location is considered at the exit hole of the vortex generator, where the predicted velocity is 1.82 m/s. There is a large pressure drop potential at that turbine location. The turbine can capture some of that flow energy and convert it to mechanical power, then electricity through a generator.

The dynamic pressure change in a no-load condition represents the total pressure difference, which can be an indication to the appropriate turbine location. Figure 9 shows how the turbine location for Case-3 of the SVE is comparable in behavior to the SCPP in terms of the dynamic pressure, while Cases 1 and 2 aren't. High dynamic pressure is seen at the vortex generator's upper hole which is comparable to the chimney's inlet. The vortex generator can replace to the high chimney solving technical and financial problems. The diameter of the vortex generator is larger, but this would not impose any problem as the height of the chimney is the main challenge when constructing SCPPs. As for the lower part of the vortex generator, there is no significant change in the dynamic pressure, even when considering the 0.45 m inner diameter orifice plate.

As mentioned earlier, the power generation unit in this study is considered as a thin disk without the actual geometry of the wind turbine. If an actual turbine is considered in an experimental model or a CFD simulation, it is suggested that a short cylindrical structure is added at the upper hole to house the turbine and bound it, removing the effect of the Betz limit.

5.3. SVE Performance Analysis

The power output and turbine effect on the generated air vortex is investigated in this section. Figure 10 shows the velocity streamlines of the air as it flows along the system. It clearly shows the system's capability in generating the air vortex. The pressure drop across the turbine does not seem to affect the vortex generation, maintenance or stability. The vortex generator accelerates the airflow from 0.13 m/s at the inlet to 1.82 m/s at the outlet. The vortex generator increased the air velocity by 14 times.

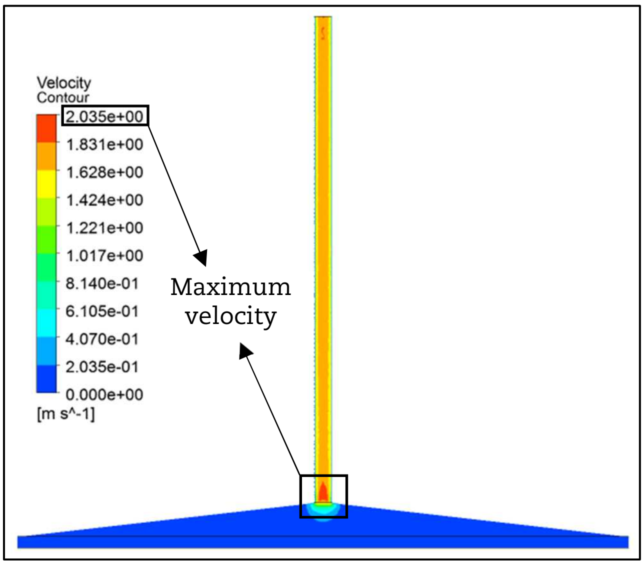

Fig. 8. Velocity contours for Case-3 of the SCPP.

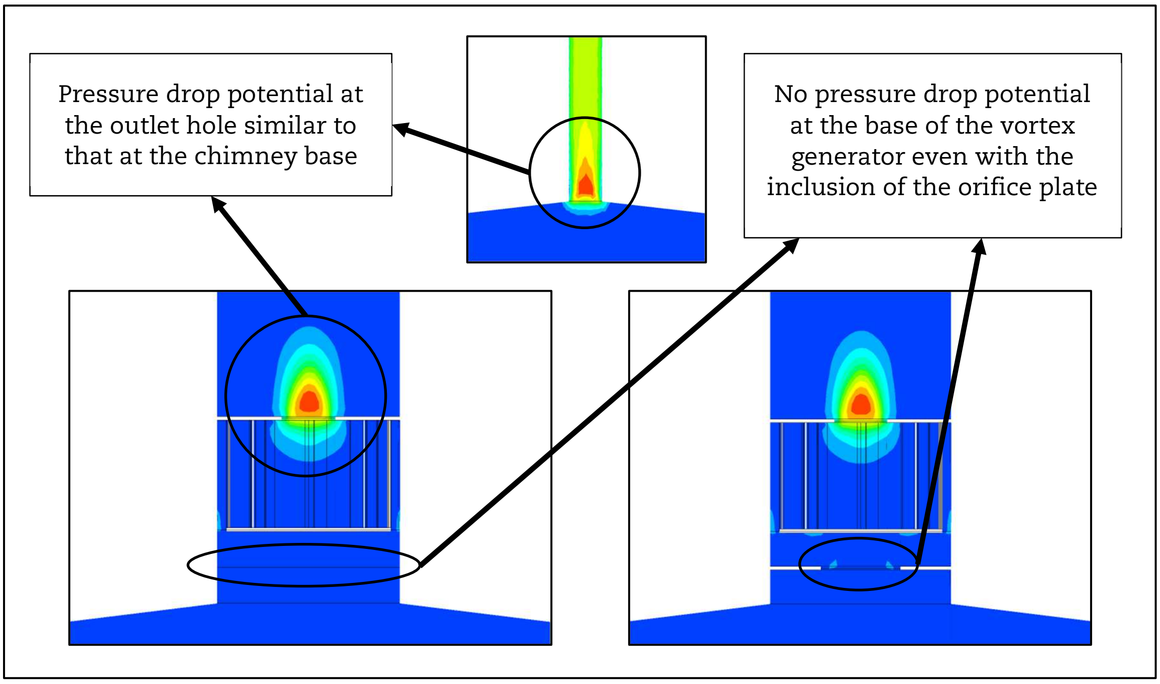

Fig. 9. Turbine pressure drop potential at the vortex generator's exit compared to the air behavior at the inlet of the solar chimney.

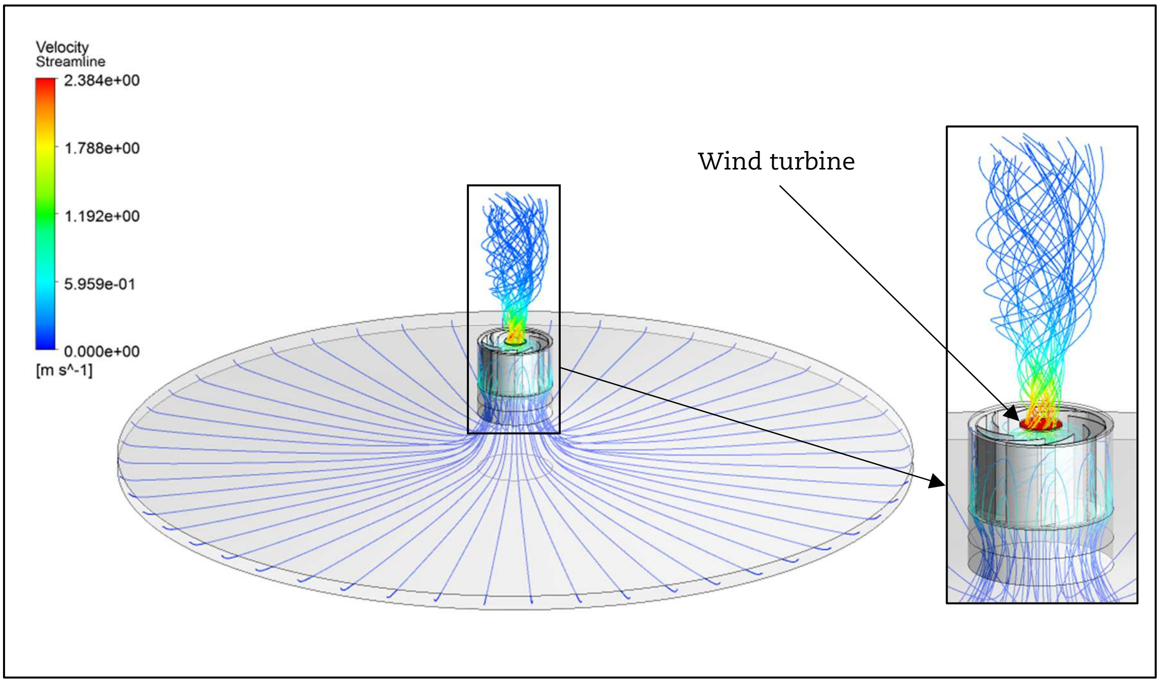

Fig. 10. Velocity streamlines of the air.

The power output variation, calculated from Eq. (16), is shown in Fig. 11. The incident solar radiation values are also presented in the same figure. The power output increases with the increase in the available incident solar radiation. The turbine power output is directly proportional to the incident solar radiation. The highest power output of 0.1 W is achieved at 1:00 PM with an incident solar radiation of 920 W/m^2. In comparison, the lowest power output is 0.01 W and was obtained at 9:00 AM with an incident solar radiation of 288 W/m^2. By further inspection of Fig. 11, it can be seen that the power output at 4:00 PM is very close to that that at 11:00 AM despite the incident solar radiation being much lower at 4:00 PM. This is attributed to the effect of the energy storage layer of the ground. The ground stores some of the energy provided to it from the solar radiation during certain hours at the morning. This is known as the charging stage of the thermal energy storage system. At the afternoon period the solar radiation starts decreasing and at a certain time the ground starts releasing the stored energy to the air compensating for the low inlet air temperature. This is called the discharging stage of the thermal energy storage system. The period between the charging and discharging stages, when the ground is neither storing more thermal energy nor releasing it, is known as the storing stage. The effect of the energy storage becomes very noticeable at the end of the afternoon at 4:00 PM as the ambient air is much colder than the ground and the solar energy input is low.

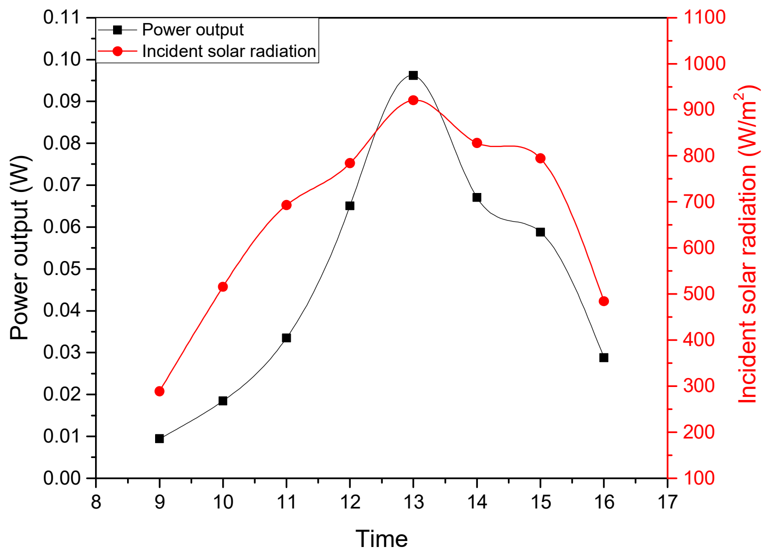

Fig. 11. Variation of power output and incident solar radiation along the operation period.

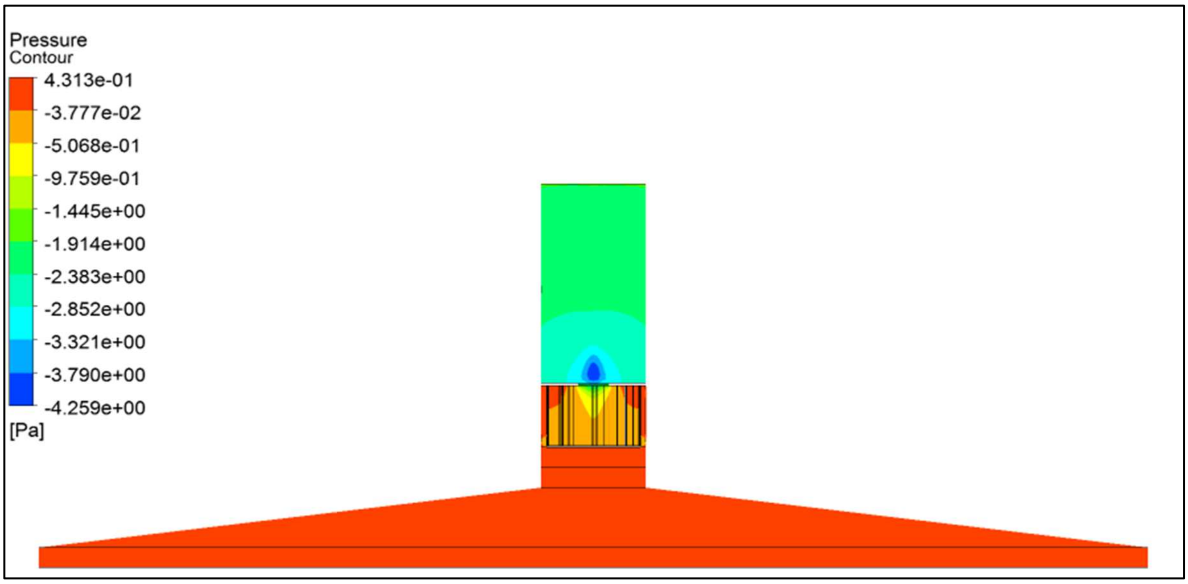

Fig. 12. Variation of the static pressure of the air along the system.

The behavior of the physical properties of the air was found to be the same with and without a turbine pressure drop, though a difference in the values of some properties was observed. So, the contours of the air properties will be presented for the case with a turbine unit, while graphical results will show the difference in values between the with turbine and without turbine cases.

The contours of static pressure are shown in Fig. 12. No observable static pressure drop occurs until the vortex generation region. It then drops significantly with the generation of the air vortex. The static pressure drops further at the outlet hole due to the decrease in the flow area and the presence of the turbine. The highest pressure drop value is 4.259 Pa which exists within the region right after the outlet hole where the turbine is installed. When the air reaches 0.3 m height, it continues with almost a constant pressure value.

The variation in the air velocity along the SVE is presented in Fig. 13. The velocity of the air increases as it enters the vortex generation arena. A maximum velocity of 2.384 m/s is reached at the outlet hole, and a decrease in the velocity of the air can be seen after a certain height of the vortex field. The vortex generator seems to function like a nozzle by increasing the velocity of the air while decreasing its pressure.

The temperature contours are shown in Fig. 14. The air enters with a low temperature equal to the ambient. The air temperature increases as more heat are added from the ground. The air temperature increases by 10.2°C from the inlet to the outlet of the solar collector. The air temperature increases again inside the inner cylinder of the vortex generator by absorbing heat from the interior surfaces. The air temperature increases by 1.2°C along the vortex generator. The difference in density between the air inside the system and the ambient air is the driving force for the updraft flow. So, the second heating mechanism inside the vortex generator causes the density to become lower, strengthening the air vortex.

The turbine unit affects the static pressure along the air vortex. The area-weighted average static pressure drop with and without a turbine along the air vortex is presented in Fig. 15. The turbine unit significantly affects the drop in static pressure. The difference between the two cases remains the same as the height of the air vortex increases. The mean difference value between the two cases is 0.67 Pa. Overall, the static pressure drop is preserved for both cases, with a slight decrease that does not seem to affect the sustainability of the vortex field. The vortex flow should continue until the static pressure drop becomes zero, meaning that mechanical equilibrium with the surrounding atmosphere is reached.

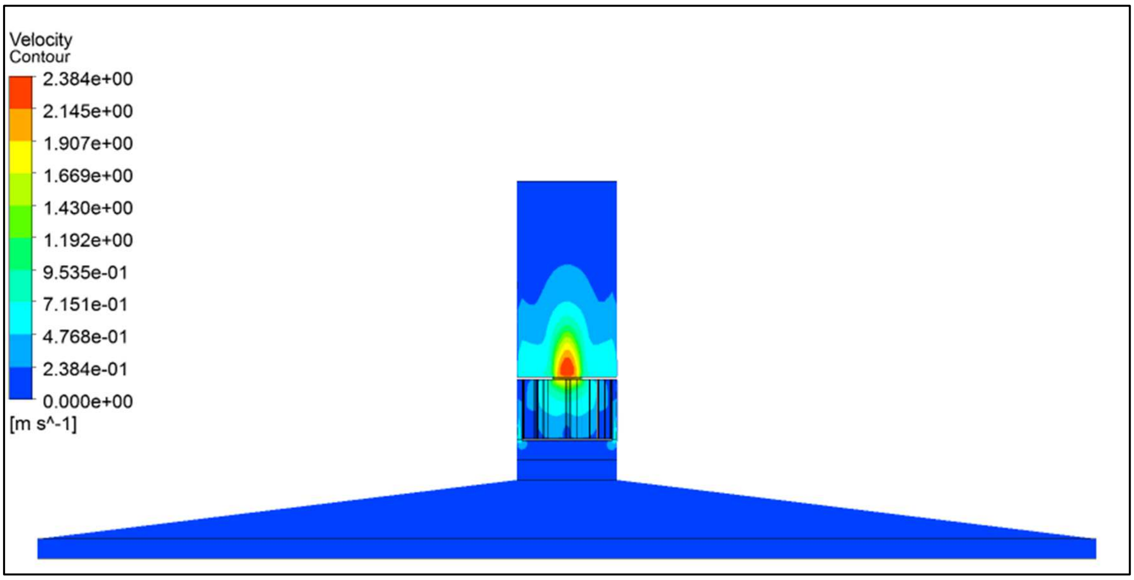

Fig. 13. Variation of the velocity of the air along the system.

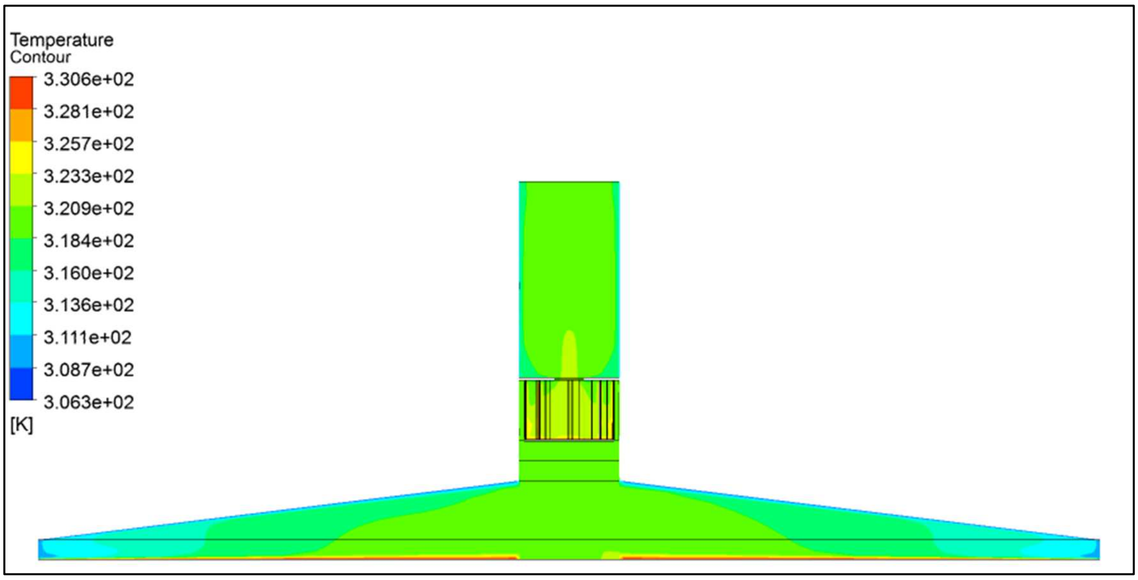

Fig. 14. Variation of the temperature of the air along the system.

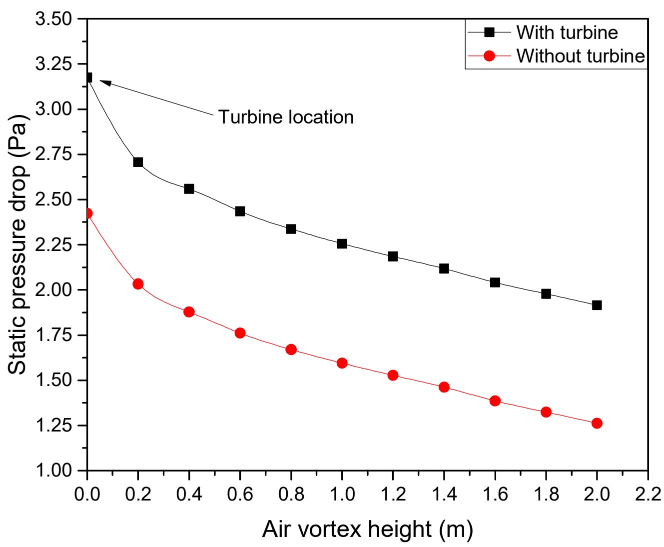

Fig. 15. Effect of the turbine on the static pressure drop inside the air vortex.

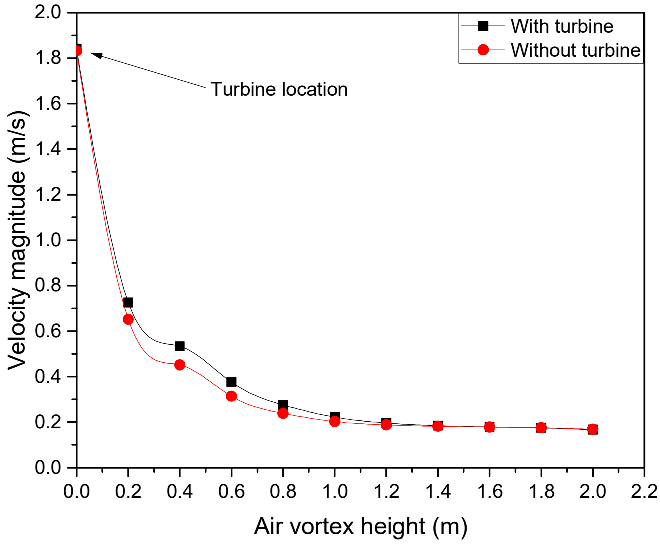

Fig. 16. Effect of the turbine on the velocity magnitude inside the air vortex.

Figure 16 shows the variation in the area-weighted average velocity magnitude along the height of the air vortex domain. The air velocity increases slightly with the consideration of the turbine unit. This is due to the drop in pressure which is inversely proportional to the velocity magnitude. Yet, the change in air velocity is small and insignificant compared to the change in static pressure. The difference between the two cases diminishes with the increase in height. At 1.2 m, the difference in values becomes very close and unrecognizable. The mean difference value for the velocity magnitude between the two cases is 0.026 m/s. In both cases, the maximum velocity is reached inside the outlet hole, then a very significant decrease is observed at 0.2 m height. The air velocity magnitude continues decreasing until 1.2 m vortex height where it continues with a very slight decrease showing almost constant values on the graph.

6. Conclusions

CFD simulations for the SVE that consider the entire system, including an exterior vortex domain, were presented. The appropriate turbine location for the SVE was investigated by comparison with three cases of the SCPP. The best location for the wind turbine is at the outlet hole as the air velocity is high and a pressure drop potential is available at that location. In addition, the turbine will be bounded and not restricted by the Betz limit. The velocity of the air at the outlet hole is 1.82 m/s compared to 1.56 m/s at the base of the chimney. The vortex generator can be a suitable replacement to the tall chimney structure as it is less expensive and easier to construct. The turbine power output is directly proportional to the incident solar radiation. However, at 4:00 PM the discharged thermal energy from the ground affects the value of the power output when the incident solar radiation is low.

There is a high drop in static pressure as the vortex flow is created, and a higher drop at the outlet hole. The air velocity increases as the vortex flow starts and reaches its peak at the outlet hole. The vortex generator increases the air velocity by 14 times. The velocity magnitude and static pressure change when the turbine unit is considered. A high decrease in static pressure occurs across the turbine with a mean difference value of 0.67 Pa. The static pressure drop is directly proportional to the system's power output. At the same time, the velocity magnitude increases due to the inverse relationship between velocity and pressure. The latter effect is insignificant as it has a mean difference value of 0.026 m/s along the air vortex, and it almost fades at 1.2 m vortex height.

Author Contributions

All authors contributed to the conceptualization and methodology of the study. Ali M. Tukkee collected the experimental data, performed the CFD simulation and wrote the original draft. Hussain H. Al-Kayiem provided the experimental system, supervised the work and reviewed and edited the manuscript. Syed I.U. Gilani supervised the work and reviewed and edited the manuscript. All authors discussed the results, reviewed, and approved the final version of the manuscript.

Acknowledgments

The authors would like to acknowledge Universiti Teknologi PETRONAS for the financial support and for granting the access to its research facilities that allowed the completion of this work.

Conflict of Interest

The authors declared no potential conflicts of interest concerning the research, authorship, and publication of this article.

Funding

This research was accomplished through the financial support of Universiti Teknologi PETRONAS with the research grant: YUTP – FRG, CS: 015LC0-404.

Data Availability Statements

Not Applicable

Nomenclature

a, b, c	Constants of the polynomial equation	S	Modulus of the strain tensor
C_1	Variable	$S_m, S_h, S_k, S_\varepsilon$	Source terms
$C_2, C_{1\varepsilon}$	Constants	T	Temperature [K]
$C_{3\varepsilon}$	Buoyancy effect on the dissipation rate	T_o	Ambient temperature [K]
C_p	Specific heat [J/kg·K]	T_{sky}	Sky temperature [K]
C_μ	Variable of eddy viscosity formula	V	Velocity [m/s]
E	Energy [J]	$\vec{v}$	Velocity vector [m/s]
$\vec{F}$	Forces	$\dot{V}$	Volumetric flowrate [m^3/s]
g	Acceleration of gravity [m/s^2]	V_w	Wind velocity [m/s]
G_k, G_b	Turbulence kinetic energy generation terms	Y_M	Contribution to the overall dissipation rate
h	Enthalpy [J] – Convection heat transfer coefficient [W/m^2·K]		**Greek Symbols**
J	Species	ΔP	Pressure drop [Pa]
k	Turbulence kinetic energy [m^2/s^2]	ε	Kinetic energy dissipation rate [m^2/s^3]
M_w	Molecular mass [kg/mol]	η	Efficiency
p	Pressure [Pa]	μ	Dynamic viscosity [N.s/m^2]
P	Power output [W]	ν	Kinematic viscosity [m^2/s]
p_{op}	Operating pressure [Pa]	ρ	Density [kg/m^3]
Pr	Prandtl number	$\sigma_k, \sigma_\varepsilon$	Turbulent Prandtl numbers
R_u	Molar gas constant [J/mol·K]	$\bar{\bar{\tau}}$	Stress tensor [N/m^2]

References

[1] Al-Kayiem, H.H., Aja, O.C., Historic and recent progress in solar chimney power plant enhancing technologies, *Renewable and Sustainable Energy Reviews*, 58, 2016, 1269-1292.
[2] Haaf, W., Friedrich, K., Mayr, G., Schlaich, J., Solar chimneys part I: principle and construction of the pilot plant in Manzanares, *International Journal of Solar Energy*, 2(1), 1983, 3-20.
[3] Haaf, W., Solar chimneys: part ii: preliminary test results from the Manzanares pilot plant, *International Journal of Sustainable Energy*, 2(2), 1984, 141-161.
[4] Schlaich, J.R., Bergermann, R., Schiel, W., Weinrebe, G., Design of commercial solar updraft tower systems—utilization of solar induced convective flows for power generation, *Journal of Solar Energy Engineering*, 127(1), 2005, 117-124.
[5] Michaud, L.M., Proposal for the use of a controlled tornado-like vortex to capture the mechanical energy produced in the atmosphere from solar energy, *Bulletin of the American Meteorological Society*, 1975, 530-534.
[6] Michaud, L.M., The atmospheric vortex engine, *In 2009 IEEE Toronto International Conference Science and Technology for Humanity (TIC-STH)*, 2009, 971-975.
[7] Natarajan, D., *Numerical simulation of tornado-like vortices*, Ph.D. Thesis, Department of Civil and Environmental Engineering, University of Western Ontario, Ontario, Canada, 2011.
[8] Ninic, N., Nizetic, S., *Solar power plant with short diffuser*, patent WO2009/060245 A, 1, 2009.
[9] Nižetić, S., Penga, Ž., Arıcı, M., Contribution to the research of an alternative energy concept for carbon free electricity production: Concept of solar power plant with short diffuser, *Energy Conversion and Management*, 148, 2017, 533-553.
[10] Penga, Ž., Nižetić, S., Arıcı, M., Solar plant with short diffuser concept: Further improvement of numerical model by included influence of guide vane topology on shape and stability of gravitational vortex, *Journal of Cleaner Production*, 212, 2019, 353-361.
[11] Zhang, M., Luo, X., Li, T., Zhang, L., Meng, X., Kase, K., Wada, S., Yu, C.W., Gu, Z., From dust devil to sustainable swirling wind energy, *Scientific Reports*, 5(1), 2015, 8322.
[12] Mohiuddin, A., Uzgoren, E., Computational analysis of a solar energy induced vortex generator, *Applied Thermal Engineering*, 98, 2016, 1036-1043.
[13] Simpson, M.W., Pearlstein, A.J., Glezer, A., Power generation from concentrated solar-heated air using buoyancy-induced vortices, *In Proceedings of the ASME 2012 6th International Conference on Energy Sustainability*, San Diego, CA, USA, 44816, 2012.
[14] Al-Kayiem, H.H., Mustafa, A.T., *Solar Vortex Engine*, Malaysia Patent, PI2015702890, 2015.
[15] Al-Kayiem, H.H., Mustafa, A.T., Gilani, S.I., Solar vortex engine: Experimental modelling and evaluation, *Renewable Energy*, 121, 2018, 389-399.
[16] Al-Kayiem, H.H., Mustafa, A.T., Gilani, S.I., Vortex field simulation and analysis of a solar updraft power engine, *WIT Transactions on Ecology and the Environment*, 205, 2016, 193-202.
[17] Das, P., Chandramohan, V.P., Performance evaluation of solar vortex engine and optimization of number of air entry slots and turbine location, *Energy Sources, Part A: Recovery, Utilization, and Environmental Effects*, 2020, 1-17.
[18] Das, P., Chandramohan, V.P., Estimation of flow parameters and power potential of solar vortex engine (SVE) by varying its geometrical configurations: A numerical study, *Energy Conversion and Management*, 223, 2020, 113272.
[19] Ismaeel, A., Al-Kayiem, H.H., Baheta, A., Aurybi, M., Numerical analysis on the influence of inflow guide vanes in A solar vortex power generator, *WIT Transactions on Ecology and the Environment*, 224, 2017, 553-563.
[20] Ismaeel, A.A., Al-Kayiem, H.H., Baheta, A.T., Aurybi, M.A., CFD modeling of artificial vortex air generator for green electric power, *In MATEC Web of Conferences*, 131, 2017, 02009.
[21] Al-Kayiem, H.H., Tukkee, A.M., Gilani, S.I., Assessment of the Design Influence of the Vortex Generator on the Performance of the Solar Vortex Engine, *Energy Conversion and Management: X*, 16, 2022, 100283.
[22] Tukkee, A.M., Al-Kayiem, H.H., Gilani, S.I., Humidity Effect on the Simulation Accuracy of Solar Vortex Engine Performance, *Journal of Solar Energy*

Research Updates, 8, 2021, 118-129.
[23] Tukkee, A.M., Al-Kayiem, H.H., Gilani, S.I., Effect of Density Variation Method and Air Humidity Consideration on the Computational Simulation of Solar Vortex Power Generation Systems, *Thermal Science and Engineering Progress*, 37, 2022, 101574.
[24] Rezaei, L., Saeidi, S., Sápi, A., Senoukesh, M.A., Gróf, G., Chen, W.H., Kónya, Z., Klemeš, J.J., Efficiency improvement of the solar chimneys by insertion of hanging metallic tubes in the collector: Experiment and computational fluid dynamics simulation, *Journal of Cleaner Production*, 415, 2023, 137692.
[25] ANSYS Fluent User's Guide 2020 R1.
[26] Ferziger, J.H., Peric, M., *Computational Methods for Fluid Dynamics*, Third ed., Springer, 2002.
[27] Jamaludin, N., Mohammed, N.I., Khamidi, M.F., Wahab, S.N.A., Thermal comfort of residential building in Malaysia at different micro-climates, *Procedia-Social and Behavioral Sciences*, 170, 2015, 613-623.
[28] Saifullah, A.Z.A., Yau, Y.H., Chew, B.T., Thermal Comfort Temperature Range for Industry Workers in a Factory in Malaysia, *American Journal of Engineering Research*, 5, 2016, 152-156.
[29] Ismaeel, A.A., *Development and evaluation of artificial vortex power generator integrated with double solar absorber*, Ph.D. Thesis, Department of Mechanical Engineering, Universiti Teknologi PETRONAS, Malaysia, 2018.
[30] Aurybi, M.A., Al-Kayiem, H.H., Gilani, S.I., Ismaeel, A.A., Numerical Assessment of Solar Updraft Power Plant Integrated with External Heat Sources, *WIT Transactions on Ecology and The Environment*, 226, 2017, 657-666.
[31] Swinbank, W.C., Long-wave radiation from clear skies, *Quarterly Journal of the Royal Meteorological Society*, 89(381), 1963, 339-348.
[32] dos Santos Bernardes, M.A., Von Backström, T.W., Kröger, D.G., Analysis of some available heat transfer coefficients applicable to solar chimney power plant collectors, *Solar Energy*, 83(2), 2009, 264-275.
[33] Pretorius, J.P., Kröger, D.G., Solar Chimney Power Plant Performance, *Journal of Solar Energy Engineering*, 128, 2006, 302-311.
[34] Masseran, N., Razali, A.M., Ibrahim, K., Zin, W.W., Evaluating the wind speed persistence for several wind stations in Peninsular Malaysia, *Energy*, 37(1), 2012, 649-656.
[35] Guo, P., Li, J., Wang, Y., Liu, Y., Numerical analysis of the optimal turbine pressure drop ratio in a solar chimney power plant, *Solar Energy*, 98, 2013, 42-48.
[36] Guo, P.H., Li, J.Y., Wang, Y., Numerical simulations of solar chimney power plant with radiation model, *Renewable Energy*, 62, 2014, 24-30.
[37] Xu, G., Ming, T., Pan, Y., Meng, F., Zhou, C., Numerical analysis on the performance of solar chimney power plant system, *Energy Conversion and Management*, 52(2), 2011, 876-883.
[38] Schlaich, J., *The solar chimney: electricity from the sun*, Edition Axel Menges, 1995.
[39] Kasaeian, A., Mahmoudi, A.R., Astaraei, F.R., Hejab, A., 3D simulation of solar chimney power plant considering turbine blades, *Energy Conversion and Management*, 147, 2017, 55-65.
[40] Tingzhen, M., Wei, L., Guoling, X., Yanbin, X., Xuhu, G., Yuan, P., Numerical simulation of the solar chimney power plant systems coupled with turbine, *Renewable Energy*, 33(5), 2008, 897-905.
[41] Zuo, L., Dai, P., Yan, Z., Li, C., Zheng, Y., Ge, Y., Design and optimization of turbine for solar chimney power plant based on lifting design method of axial-flow hydraulic turbine impeller, *Renewable Energy*, 171, 2021, 799-811.
[42] Koonsrisuk, A., Chitsomboon, T., Mathematical modeling of solar chimney power plants, *Energy*, 51, 2013, 314-322.
[43] Guo, P., Li, J., Wang, Y., Wang, Y., Evaluation of the optimal turbine pressure drop ratio for a solar chimney power plant, *Energy Conversion and Management*, 108, 2016, 14-22.
[44] Guo, P., Wang, Y., Li, J., Wang, Y., Thermodynamic analysis of a solar chimney power plant system with soil heat storage, *Applied Thermal Engineering*, 100, 2016, 1076-1084.
[45] Pastohr, H., Kornadt, O., Gürlebeck, K., Numerical and analytical calculations of the temperature and flow field in the upwind power plant, *International Journal of Energy Research*, 28(6), 2004, 495-510.
[46] Zhou, X., Yang, J., Xiao, B., Hou, G., Experimental study of temperature field in a solar chimney power setup, *Applied Thermal Engineering*, 27(11-12), 2007, 2044-2050.

ORCID iD

Ali M. Tukkee https://orcid.org/0000-0002-1095-2297
Hussain H. Al-Kayiem https://orcid.org/0000-0002-6045-8553
Syed I.U. Gilani https://orcid.org/0000-0002-8430-0048

How to cite this article: Tukkee A.M., Al-Kayiem H.H., Gilani S.I.U. Assessment of the Turbine Location for Optimum Performance of the Solar Vortex Engine as a Replacement to the Tall Chimney Solar Updraft Power Plant Design, *J. Appl. Comput. Mech.*, 10(1), 2024, 38–54. https://doi.org/10.22055/jacm.2023.43942.4146